

# Crystallography without crystals I: The common-line method for assembling a 3D diffraction volume from single-particle scattering

V. L. Shneerson, A. Ourmazd, and D. K. Saldin

Department of Physics,  
University of Wisconsin-Milwaukee, P. O. Box 413,  
Milwaukee, WI 53201, U.S.A.

E-mail: valentin@uwm.edu, ourmazd@uwm.edu, dksaldin@uwm.edu

October 30, 2018

## Abstract

We demonstrate that a common-line method can assemble a 3D oversampled diffracted intensity distribution suitable for high-resolution structure solution from a set of measured 2D diffraction patterns, as proposed in experiments with an X-ray free electron laser (XFEL) (Neutze *et al.*, 2000). Even for a flat Ewald sphere, we show how the ambiguities due to Friedel's Law may be overcome. The method breaks down for photon counts below about 10 per detector pixel, almost 3 orders of magnitude higher than expected for scattering by a 500 kDa protein with an XFEL beam focused to a  $0.1 \mu\text{m}$  diameter spot. Even if  $10^3$  orientationally similar diffraction patterns could be identified and added to reach the requisite photon count per pixel, the need for about  $10^6$  orientational classes for high-resolution structure determination suggests that about  $\sim 10^9$  diffraction patterns must be recorded. Assuming pulse and read-out rates of 100 Hz, such measurements would require  $\sim 10^7$  seconds, i.e. several months of continuous beam time.

# 1 Introduction

X-ray crystallography is one of the key contributions of the physical sciences to the life sciences. Its application to biological, biochemical, and pharmaceutical problems continues to enable breakthroughs (Cramer *et al.*, 2001; Gnatt *et al.*, 2001) highlighting the importance of structure to function. However, roughly 40% of biological molecules do not crystallize, and many cannot easily be purified. These factors severely limit the applicability of X-ray crystallography; although more than 750,000 proteins have been sequenced, the structures of less than 10% have been determined to high resolution (Protein Data Bank, <http://www.pdb.org>). The ability to determine the structure of individual biological molecules - without the need for purification and crystallization - would constitute a fundamental breakthrough.

The confluence of five factors has generated intense interest in single-molecule crystallography by short-pulse X-ray scattering: a) The advent of algorithms for determining phases from measured diffraction intensities by successive and repeated application of constraints in real and reciprocal spaces (see e.g. Fienup, 1978; Elser, 2003; Millane, 2003), with demonstrations in astronomy (Fienup, 1982); diffractive imaging of nanoparticles (Williams *et al.*, 2003; Wu *et al.*, 2005; Chapman *et al.*, 2006), biological cells (Shapiro *et al.*, 2005; Thibault *et al.*, 2006); small molecule crystallography (Oszlányi and Sütö, (2003); Wu *et al.* (2004a); surface crystallography (Kumpf *et al.*, 2001; Fung *et al.*, 2007); and protein crystallography (Miao *et al.*, 2001; Spence *et al.*, 2005); b) Development of sophisticated techniques for determining the relative orientation of electron microscope images of biological entities, such as cells and large macromolecules (see e.g. Frank, 2006); c) Development of techniques for producing beams of hydrated proteins by electrospraying or Raleigh-droplet formation (Fenn, 2002; Spence *et al.*, 2005); d) The promise of very bright, ultra-short pulses of hard X-rays from X-ray Free Electron Lasers (XFELs) under construction in the US, Japan, and Europe (Normille, 2006); e) The prospect of overcoming the limits to achievable resolution due to radiation damage by using short pulses of radiation (Solem and Baldwin, 1982; Neutze *et al.*, 2000).

It has been suggested (Neutze *et al.*, 2000; Hajdu *et al.*, 2000; Abela *et al.*, 2007) that an experiment to determine the structure of a biological molecule might, in principle, proceed as follows: i) A train of individual hydrated proteins is exposed to a synchronized train of intense X-ray pulses. As a single pulse is sufficient to destroy the molecule, the pulses (and data collection) must be short compared with the roughly 50 fs needed for the molecular constituents to fly apart (Neutze *et al.*, 2000; Jurek *et al.*, 2004). ii) The two-dimensional (2D) diffraction patterns obtained with single pulses are read out, each pattern corresponding to an unknown, random orientation of the molecule. iii) The relative orientations of the molecule corresponding to 2D diffraction patterns (and hence the relative orientations of each diffraction pattern in 3D reciprocal space) are determined. iv) A noise-averaged 3D diffracted intensity distribution is constructed. v) The structure of the molecule is determined from the diffracted intensity distribution by an iterative “phasing algorithm” (Miao *et al.*,

2001).

As pointed out by Huld *et al.*, (2003), for this approach to succeed in principle, it is necessary to develop a noise-robust algorithm to determine the relative orientations of diffraction patterns obtained from randomly-oriented individual molecules, to reconstruct the 3D diffracted intensity distribution of sufficient quality, and to determine the secondary structure of individual biological molecules.

In brief, starting with a collection of noisy 2D diffraction patterns of unknown orientation, such a method recovers the 3D electron density of a molecule, providing a quantitative measure of the reliability of the reconstruction. It has been suggested that an algorithm developed for the analogous problem of the reconstructing a 3D image of a large molecule or nanoparticle from different projected electron microscope images, the method of common lines, may be employed for this task. We investigate the capabilities and limitations of such an approach for structure recovery from simulated short-wavelength diffraction patterns of a small (10-residue) synthetic protein, Chignolin (Protein Data Bank Entry 1UAO).

Starting with 630 simulated, noise-free 2D diffraction patterns of 0.1 Å wavelength X-rays from random orientations of the molecule, we show that such an algorithm is able to recover the electron density distribution of the (small) test protein molecule, Chignolin, up to about 1 Å resolution with a fidelity measured by a correlation coefficient of 0.7 between the model and recovered electron density distributions. This constitutes the first demonstration of an integrated algorithm able to perform all the tasks necessary to extract a molecular electron density from a set of 2D diffraction patterns of random unknown orientations. We have also investigated the limits of the algorithm with respect to shot noise (modeled by Poisson statistics) in the detected signal. Our results show that the common-line method requires at least 10 photons/pixel. This is at least two orders of magnitude higher than the anticipated signal levels from the LCLS XFEL currently under construction.

The algorithm consists of three primary modules: a) Determination of the relative orientations of the measured diffraction patterns in 3D reciprocal space; b) From the resulting irregular distribution of diffracted intensities, application of a gridding algorithm to generate data on a uniform rectilinear grid in reciprocal space; c) Application to this gridded data of a 3D iterative algorithm to find the phases associated with the grid intensities, and recover the 3D electron density of the molecule. For an experiment which provided independent information about the orientations of the sample, steps b) and c) were previously implemented by Chapman *et al.* (2006).

## 2 Determination of the Relative Orientations of the Diffraction Patterns

In the following, we assume that the X-ray energy is high enough, and the solid angle subtended by the diffraction pattern at the sample small enough that it is a reasonable

approximation to consider each diffraction pattern as a planar central section through the 3D reciprocal space of the molecule. In practice, this is valid for X-ray wavelengths of about 0.1 Å. Then, the problem reduces to determining the relative orientations of these planar sections from the data in the diffraction patterns alone without any knowledge of the structure of the molecule. For longer wavelengths, as pointed out previously (e.g. Huldt *et al.*, 2003, Chapman, 2007), it will be necessary to take account of the curvature of the Ewald sphere, when the common lines become arcs of a circle rather than straight lines. The extra complexity of identifying such arcs may be offset by two factors: (1) the avoidance of ambiguities stemming from the duplication of intensities in the same 2D diffraction pattern, due to Friedel’s Law (see below); and (2) the possibility of determining all three Euler angles relating the orientations of any two diffraction patterns from just their mutual common line (Huldt, *et al.*, 2003), if the extra parameter of the radius of curvature of the common arcs may be determined with sufficient accuracy.

Our approach is inspired by the analogous problem of reconstructing the 3D structure of a macromolecule or nanoparticle from electron microscope images representing projections of copies of the object along random directions (Frank, 2006). This problem has been solved by exploiting the central section theorem (Farrow and Ottensmeyer, 1992), and has been developed most notably by these authors and also previously by van Heel (1987); and Goncharov *et al.*, (1987). From the *projection-slice theorem*, the Fourier transform of a 2D (i.e. projected) image is a central slice through the complex 3D reciprocal space of the 3D object. Any two central sections intersect along a line. This allows partial alignment of the two central sections with respect to each other. Specifically, determination of the gradients of this common line relative to, say, 2D Cartesian coordinate systems in the planes of each of the central sections allows two of the three Euler angles specifying the relative orientations of these central sections to be deduced. Using this procedure, it is generally possible to determine six of the nine interplanar Euler angles between *three* independent diffraction patterns. Knowledge of these six Euler angles allows the remaining three to be deduced by geometrical construction.

We point to one important difference between an application of the common-line approach to images (as in 3D electron microscopy) and diffraction patterns. The images constitute projections of the object in real space. Some applications of the central section theorem have been performed in reciprocal space, exploiting the fact that 2D Fourier transforms of these images yield moduli and phases of *complex* amplitudes on central sections through reciprocal space. Sinograms of the data of any two diffraction patterns allow the unique identification of a pair of Euler angles relating the two central sections in 3D reciprocal space (Frank, 2006). In contrast, in our problem, the raw experimental data are diffracted intensities, and direct information is available only about the *moduli* of the complex amplitudes in reciprocal space.

Friedel’s Law of crystallography suggests that the intensity distribution along a radial line through the center of each diffraction pattern is the same as one rotated relative to it by 180°. This means that, for a flat Ewald sphere, the determination of

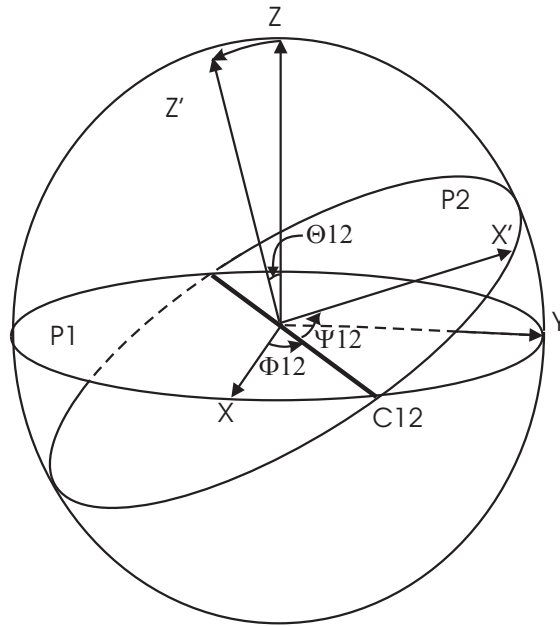


Figure 1: Transformation of central section  $P1$  into  $P2$ , by rotation through Euler angles  $\Phi_{12}$ ,  $\Theta_{12}$ , and  $\Psi_{12}$ .

the pair of Euler angles from common lines is uncertain by  $\pm 180^\circ$ . Any significant curvature of the Ewald sphere removes this ambiguity, but even for a flat Ewald sphere, this uncertainty may be resolved through consistency conditions amongst the Euler angles, as shown below.

## 2.1 Determination of two Euler angles between two intersecting diffraction patterns

Fig. 1 illustrates the reciprocal-space geometry of two central sections, representing diffraction patterns,  $P1$  and  $P2$ . Let the Euler angles relating  $P1$  and  $P2$  be  $\Phi_{12}$ ,  $\Theta_{12}$ , and  $\Psi_{12}$ . Consider three Cartesian axes  $X$ ,  $Y$ , and  $Z$ , where  $X$  and  $Y$  lie in the plane of  $P1$ , and  $Z$  is normal to it. Diffraction pattern  $P2$  is related to  $P1$  by a set of three rotations. The initial rotation is through the azimuthal angle  $\Phi_{12}$  about the  $Z$  axis. Next follows a rotation through  $\Theta_{12}$  about the  $X$  axis obtained after the first rotation. Let us denote this axis by  $C12$ . The final rotation is through  $\Psi_{12}$  about the new  $Z$  axis, denoted  $Z'$ . It is clear from the figure that  $C12$  is the line of intersection between  $P1$  and  $P2$ , i.e the common line.

The orientation of the common line  $C12$  relative to the  $(X,Y)$  Cartesian axes in the plane of  $P1$  is shown in Fig. 2. The gradient  $m_{12}$  of  $C12$  with respect to the

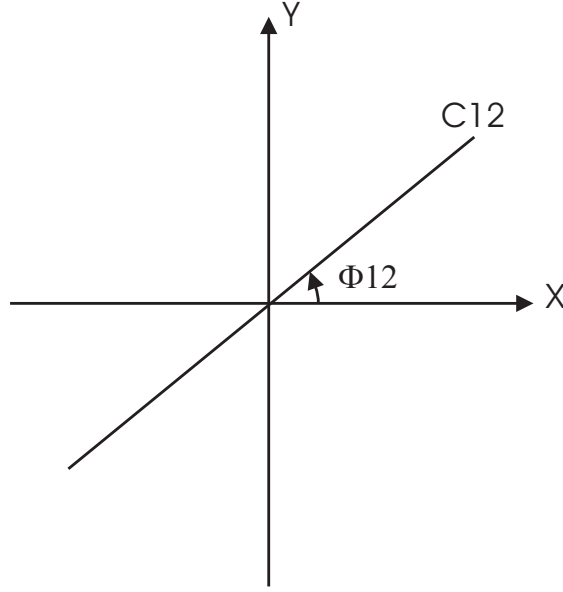


Figure 2: *Orientation of common line C12 relative to the Cartesian axes (X,Y) in central section P1.*

(X,Y) axes in the plane of P1 is given by

$$m_{12} = \tan (\Phi_{12}) \quad (1)$$

and hence the Euler angle

$$\Phi_{12} = \arctan (m_{12}) \quad (2)$$

can be determined if the common line C12, and hence its gradient in the plane of P1 relative to the Cartesian axes (X,Y) can be identified.

Now note that since C12 is the common line, it must also be contained in the plane of P2 after the Euler-angle rotations. Its orientation relative to the Cartesian axes (X',Y') in the plane of P2 is depicted in Fig. 3. Its gradient  $m_{21}$  relative to the axes (X',Y') in P2 is

$$m_{21} = -\tan (\Psi_{12}) \quad (3)$$

and hence the Euler angle

$$\Psi_{12} = \arctan (-m_{21}) \quad (4)$$

may be determined if the common line C12, and hence its gradient in the plane of P2 relative to the Cartesian axes (X',Y') can be identified in the diffraction pattern in that plane.

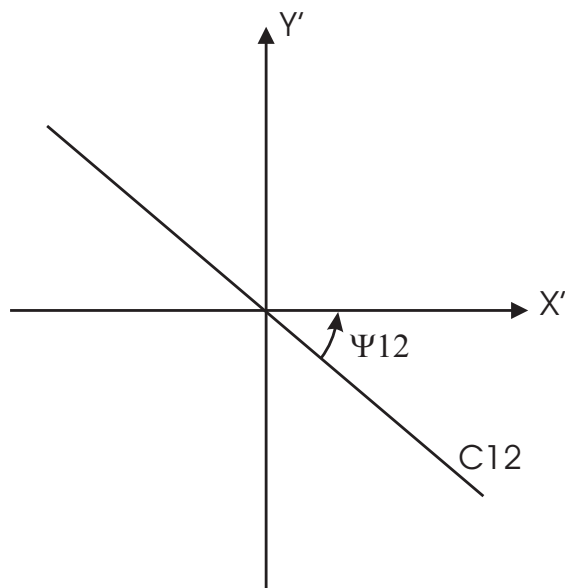


Figure 3: Orientation of common line  $C12$  relative to the Cartesian axes  $(X', Y')$  after the Euler-angle rotations in the diffraction pattern  $P2$ .

Given two diffraction patterns, a pairwise numerical comparison (*sinogram* comparison, Frank, 2006) of the intensity distributions along radial directions of the two patterns may be conducted. An automated criterion, such as an R-factor, monitors the degree of agreement. An exhaustive search is performed of all pairs of radial distributions of the intensities on the two patterns. A global minimum of the R-factor is assumed to determine the common line. For the diffraction patterns  $P1$  and  $P2$  above, denote the common line by  $C12$ . This gives estimates of the Euler angles  $\Phi12$  and  $\Psi12$ .

Fig. 4(a) and (b) show two simulated diffraction patterns ( $40 \times 40$  pixels) from random orientations of our test protein, Chignolin. The maximum lateral wavevector in the direction of the x-axis was 10 times the Nyquist frequency for the assumed lateral extension of the protein ( $16 \text{ \AA}$ ). This corresponds to a reciprocal-space length of  $q = 2\pi(10)/16 = 3.93 \text{ \AA}^{-1}$ . The wavevector,  $k$ , of 124 keV hard X-rays is about  $63 \text{ \AA}^{-1}$ . The scattering angle corresponding to the middle of an edge of the square diffraction pattern was calculated from  $2 \arcsin(q/2k) = 3.2^\circ$ . The central part of each diffraction pattern contains high intensities of relatively low detail, but several orders of magnitude stronger than in the outer parts of the pattern containing the high-resolution structural information. A numerical search for the common lines between the two patterns of Fig. 4 was performed by pairwise comparisons of the radial intensity distributions from the two patterns in angular steps of  $1^\circ$ , excluding the pixels within a central high-intensity disc of 7-pixel radius corresponding to a scattering angle of  $\sim 1^\circ$ . Effectively, the values of the azimuthal Euler angles  $\Phi12$  and  $\Psi12$  were identified by a contour plot of the form shown in Fig. 5 The identified

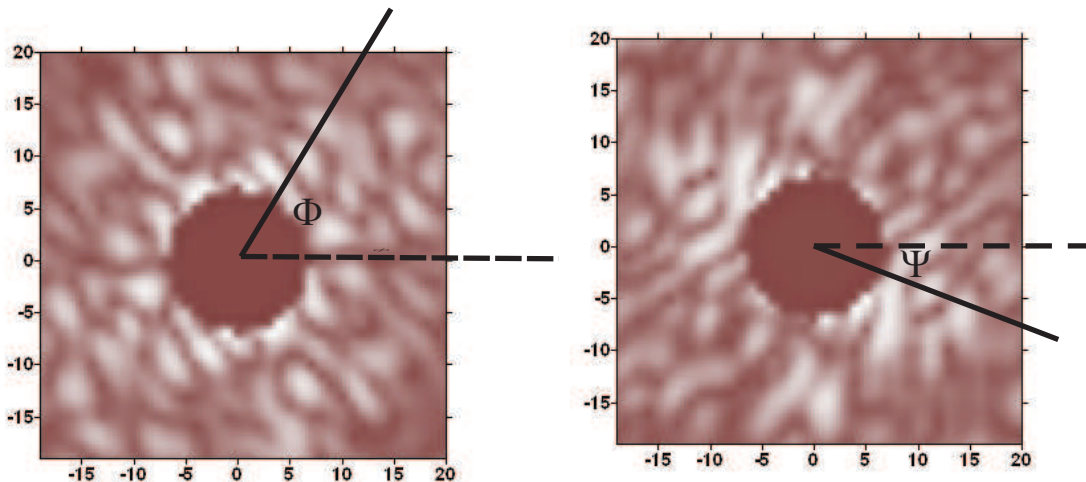


Figure 4: *Identification of the common line in two typical simulated diffraction patterns from a model of the protein Chignolin, leading to a determination of the azimuthal Euler angles  $\Phi$  and  $\Psi$  relating the 3D orientations of the diffraction patterns.*

common lines are also shown in Fig. 4(a) and (b). Due to the Friedel Law degeneracy mentioned above, any  $180^\circ$  range of azimuthal angles would be expected to contain such a minimum. For convenience, we perform numerical searches for  $\Phi_{12}$  and  $\Psi_{12}$  angles over an azimuthal angle range of 0 to  $180^\circ$ . Then Friedel’s Law suggests equally valid values for these angles of  $\Phi_{12} + 180^\circ$  and  $\Psi_{12} + 180^\circ$ , respectively. Without phase information, it is impossible to tell from the diffraction data alone, which of the two values of each angle is “correct”.

In the case of the flat Ewald sphere considered here, it is not possible to determine the Euler angle  $\Theta_{12}$  between the normals to these planes with the data in the diffraction patterns  $P_1$  and  $P_2$  alone. In order to determine that angle, it is necessary to have diffraction data in at least one more distinct reciprocal-space plane, which intersects the planes of  $P_1$  and  $P_2$  along two further distinct common lines.

## 2.2 Determination of all nine Euler angles relating three general central sections

Let  $P_3$  denote a third diffraction pattern (Fig. 6). Since each diffraction pattern forms a central section through reciprocal space, each pair of diffraction patterns intersect along a common line, with the three common lines intersecting at the origin ( $O$  in Fig. 6). Denote the Euler angles specifying the transformation of the plane of  $P_2$  to that of  $P_3$  by  $(\Phi_{23}, \Theta_{23}, \Psi_{23})$ , and those transforming plane of  $P_3$  to that of  $P_1$  by  $(\Phi_{31}, \Theta_{31}, \Psi_{31})$ . In the notation of Fig. 6, the common line between  $P_1$  and  $P_2$  is denoted by  $OC$ , that between  $P_2$  and  $P_3$  by  $OA$  and that between  $P_3$  and  $P_1$



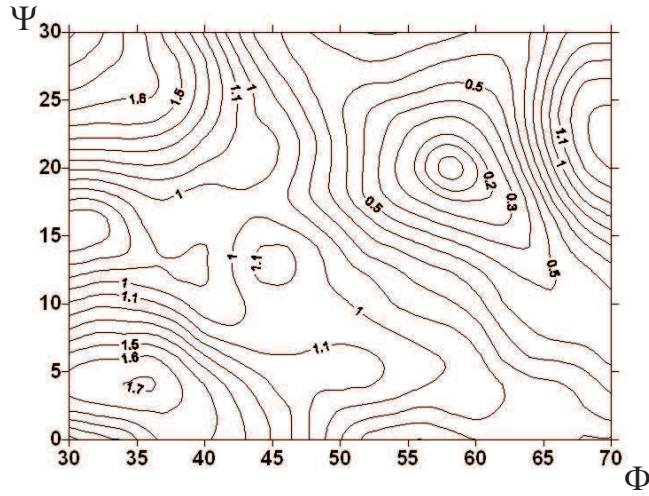


Figure 5: *Contour map of sinogram comparisons between the two diffraction patterns of Fig. 4 in the vicinity of the global minimum at  $\Phi=58^\circ$ ,  $\Psi=21^\circ$ .*

by  $OB$ , with  $A$ ,  $B$ , and  $C$  representing points on the surface of a unit sphere centered on  $O$ .

By analogy with the method described in the last section, a comparison of the diffraction intensities of  $P2$  and  $P3$  can determine the Euler angles  $\Phi23$  and  $\Psi23$ . Likewise comparison of the data of  $P3$  and  $P1$  can determine the angles  $\Phi31$  and  $\Psi31$ . This leaves only three angles to be determined:  $\Theta12$  between  $P1$  and  $P2$ ;  $\Theta23$  between  $P2$  and  $P3$ ; and  $\Theta31$ , between  $P3$  and  $P1$ .

The geometrical construction of Fig. 6 shows that the remaining Euler angles are the vertex angles  $\angle ACB$ ,  $\angle BAC$ , and  $\angle CBA$  of the spherical triangle  $ABC$  on the surface of the unit sphere. Also note that the lengths of the sides of this spherical triangle (the arcs  $CB$ ,  $BA$ , and  $AC$ ) are equal to the sums of angles  $\Psi31 + \Phi12 = \alpha_{312}$  (say),  $\Psi12 + \Phi23 = \alpha_{123}$  (say), and  $\Psi23 + \Phi31 = \alpha_{231}$  (say), respectively (expressed in radians). (For example, if we consider a transformation from plane 3 to plane 1 followed by one from plane 1 to plane 2, then the third Euler angle in the former transformation ( $\Psi31$ ) and the first Euler angle in the latter transformation ( $\Phi12$ ) involve rotations in the same plane, that of  $P1$ .)

The *cosine rule* of spherical trigonometry gives

$$\cos (AB) = \cos (CA) \cos (CB) + \sin (CA) \sin (CB) \cos (\angle ACB) \quad (5)$$

that is,

$$\cos \alpha_{231} = \cos \alpha_{123} \cos \alpha_{312} + \sin \alpha_{123} \sin \alpha_{312} \cos (\Theta12) \quad (6)$$

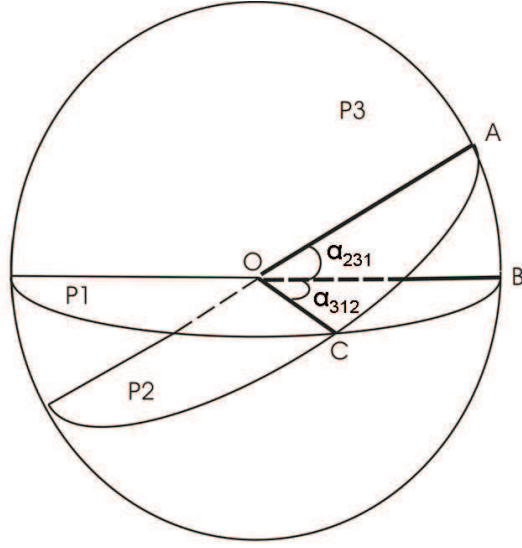


Figure 6: Geometrical construction for determining the relative Euler angle  $\Theta_{12}$  between diffraction patterns  $P1$  and  $P2$ , given the six Euler azimuthal angles  $\Phi$  and  $\Psi$  relating  $P1$ ,  $P2$  and  $P3$ .

and thus

$$\Theta_{12} = \arccos \left[ \frac{\cos \alpha_{231} - \cos \alpha_{123} \cos \alpha_{312}}{\sin \alpha_{123} \sin \alpha_{312}} \right]. \quad (7)$$

This expression was obtained by Goncharov *et al.* (1987) by a different argument.

Generalizing this result for a triplet of diffraction patterns  $i$ ,  $j$ , and  $k$ , the angle  $\Theta_{ij}$  between  $i$  and  $j$ , is given by

$$\Theta_{ij} = \arccos \left[ \frac{\cos \alpha_{jki} - \cos \alpha_{ijk} \cos \alpha_{kij}}{\sin \alpha_{ijk} \sin \alpha_{kij}} \right], \quad (8)$$

where

$$\alpha_{ijk} = \Psi_{ij} + \Phi_{jk}, \quad (9)$$

$$\alpha_{kij} = \Psi_{ki} + \Phi_{ij}, \quad (10)$$

and

$$\alpha_{jki} = \Psi_{jk} + \Phi_{ki} \quad (11)$$

Pair	$\Phi$	$\Psi$
(1,2)	16.0	108.0
(2,3)	173.0	174.0
(3,1)	121.0	132.0

Table 1:  $\Phi$  and  $\Psi$  Euler angles (in degrees) relating diffraction patterns from three random orientations of the molecule, as determined by numerical sinogram comparisons.

with  $k$  a third plane.

The above analysis shows that, provided the Euler angles  $\Phi$  and  $\Psi$  specifying the directions of common lines between any three sets of diffraction patterns  $i$ ,  $j$ , and  $k$  are determined (e.g., by comparisons of sinograms from the diffraction patterns), the Euler angles  $\Theta$  about the ‘‘hinge axes’’ formed by the common lines amongst those diffraction patterns can be deduced by the analytic formula (8).

### 2.3 Removal of the ambiguities due to Friedel’s Law

As pointed out in the previous section, the Euler angles  $\Phi$  and  $\Psi$  may be determined from the diffraction pattern data only to modulo  $180^\circ$ , due to Friedel’s Law. Thus, in addition to initial values (in the range 0 to  $180^\circ$ ) assigned to these angles by the automated numerical sinogram comparison, one must also consider as possible values of these angles,  $\Phi + 180^\circ$  and  $\Psi + 180^\circ$ , respectively. The possibility of two values for each of the three  $\Phi$  angles and two for each of the three  $\Psi$  angles, implies four possible values of each of the  $\alpha$  angles in expressions (9), (10), and (11). Since three distinct  $\alpha$  angles enter into the formula (8), there are  $4^3=64$  possible values of  $\Theta_{ij}$  for a given set of  $\Phi$  and  $\Psi$  angles deduced from three different diffraction patterns.

In fact, this is not the case. Many combinations of  $\Phi$  and  $\Psi$  give rise to the same  $\Theta_{ij}$ , and a large number of combinations result in arguments of the *arccos* function in (8) outside the range of -1 to 1, giving no geometrically meaningful solution at all. This eliminates all but two sets of the three  $\Theta$  angles. The remaining ambiguity is due to the well known enantiometric ambiguity of molecular structures that give rise to the same diffraction intensities. This ambiguity is impossible to resolve from the diffraction data alone. An arbitrary but consistent choice of one of the two sets of  $\Theta$  angles produces one of the two enantiomers of the structure.

A concrete example from a simulation of three diffraction patterns, 1, 2, and 3 from random orientations of the same molecule is illustrative. The  $\Phi$  and  $\Psi$  angles of Table 1 were determined by numerical comparisons of sinograms of the three patterns.

Substituting all 64 combinations of  $\Phi$  and  $\Phi + \pi$ , and  $\Psi$  and  $\Psi + \pi$  into Eqs.(8)-(11) results in 46 combinations with values for the cosine of the relevant angle  $\Theta$  lying

Pair	$\Theta$
(1,2)	114.2
(2,3)	144.4
(3,1)	103.4

Table 2: One set of three (hinge) angles  $\Theta$  (in degrees) between the three diffraction patterns oriented in 3D reciprocal space, deduced from Eq. (8).

Pair	$\Theta$
(1,2)	19.1
(2,3)	12.1
(3,1)	159.5

Table 3: Another set of values of the same  $\Theta$  angles (in degrees) as in Table 2, as determined by the same method. This solution corresponds to the enantiomer structure.

outside the range -1 to 1. Nine of the 64 combinations give rise to the  $\Theta$  angles in Table 2.

Another 9 combinations give rise to the values for the  $\Theta$  angles in Table 3.

It turns out that the two sets of values of the  $\Theta$  angles determined by this method correspond to the two enantiometric solutions referred to above. Thus the method described rules out Friedel pair combinations of common-line directions that are unphysical, producing just the two enantiomers consistent with the diffraction data.

## 2.4 Averaging and Self-Consistency Checks

A particular angle  $\Theta_{ij}$  may be estimated from (8) by taking as the third diffraction pattern  $k$  any one of the  $N - 2$  other diffraction patterns. Each choice of third diffraction pattern will yield two possible (usually widely separated) values of  $\Theta_{ij}$ , corresponding to the two possible enantiomers. This time, since we have already chosen an enantiomer in our previous estimate of  $\Theta_{ij}$  using a different third diffraction pattern, we choose the solution that is closest to the previously selected value of  $\Theta_{ij}$ , i.e., the same enantiomer. The finally assigned value of this angle will be the average of these values computed by (8) via all possible third planes  $k$ , namely:

$$\Theta_{ij} = \frac{1}{N - 2} \sum_{k \neq i, k \neq j} \arccos \left[ \frac{\cos \alpha_{jki} - \cos \alpha_{kij} \cos \alpha_{ijk}}{\sin \alpha_{kij} \sin \alpha_{ijk}} \right]. \quad (12)$$

The calculations of the  $\Theta$  angles via (12), including the tests of enantiomeric consistency, are very rapid. The bulk of the computational time involves the sinogram comparisons for diffraction pattern pairs. The time for these computations scales as the total number of pairs amongst  $N$  diffraction patterns, namely,  $N(N - 1)/2$ . To save computational time for the 630 diffraction patterns, we divided them into sets of about 10 diffraction patterns each. So long as two diffraction patterns are common to each of these sets of about 10, the method determines the relative orientations of all diffraction patterns relative to these two for a given enantiomer, with a computational time saving of a factor of approximately  $(630/10)^2 \simeq 4000$ .

A method of sinogram matching determines common-line directions by comparison between pairs of projections/diffraction patterns at a time. Farrow and Otensmeyer (1992) have suggested a method of simultaneously taking account of data from all available projections by means of quaternion mathematics. We propose here an alternative method of ensuring that all determined Euler angles are consistent with the data of all available diffraction patterns. With noisy data, such a self-consistency condition may even help reduce some of the errors due to noise. Consider any three noncoplanar diffraction patterns,  $i$ ,  $j$ , and  $k$ . Then

$$R(\Phi_{ij}, \Theta_{ij}, \Psi_{ij})R(\Phi_{jk}, \Theta_{jk}, \Psi_{jk})R(\Phi_{ki}, \Theta_{ki}, \Psi_{ki}) = I, \quad (13)$$

where  $R$  is the 3D rotation matrix, which transforms plane  $i$  to plane  $j$  in 3D reciprocal space, and  $I$  is the 3D unit matrix. Since  $R(\Phi_{jk}, \Theta_{jk}, \Psi_{jk})^{-1} = R(\Phi_{kj}, \Theta_{kj}, \Psi_{kj})$ , and  $R(\Phi_{ki}, \Theta_{ki}, \Psi_{ki})^{-1} = R(\Phi_{ik}, \Theta_{ik}, \Psi_{ik})$ , Eq.(13) may be rewritten

$$R(\Phi_{ij}, \Theta_{ij}, \Psi_{ij}) = R(\Phi_{ik}, \Theta_{ik}, \Psi_{ik})R(\Phi_{kj}, \Theta_{kj}, \Psi_{kj}), \quad \forall k. \quad (14)$$

If the  $\Phi$  and  $\Psi$  angles on the RHS of (14) have been found by sinogram matching, and the  $\Theta$  angles on the RHS via Eq.(12), Eq. (14) may be used to update the Euler angles  $\Phi_{ij}$ ,  $\Theta_{ij}$ , and  $\Psi_{ij}$  on its LHS. Since, for given planes  $i$  and  $j$ , there are  $N - 2$  other planes  $k$ , these angles may be calculated independently from  $N - 2$  equations of the form (14), and the values averaged. A different pair of planes  $ij$  can then be selected and the procedure repeated to update the Euler angles on the LHSs of (14) relating all pairs of planes.

To summarize this section, we have described a detailed procedure for orientating in 3D reciprocal space, a large number of diffraction patterns from random unknown orientations of an object *without any knowledge of the structure of the object*. The recovery of a molecular electron density from such data requires the determination of the *phases* associated with these intensities. This may be done by the method of *oversampling* (Miao *et al.*, 2001), involving iterative Fourier transformations of the data from reciprocal to real space, and applications of appropriate constraints in each of the spaces. A conventional fast Fourier transform (FFT) algorithm (Cooley and Tukey, 1965) requires data on a regular Cartesian grid in each space. Thus, it is necessary to perform a *gridding* operation in 3D reciprocal space to prepare the data for such an iterative *phasing* algorithm.

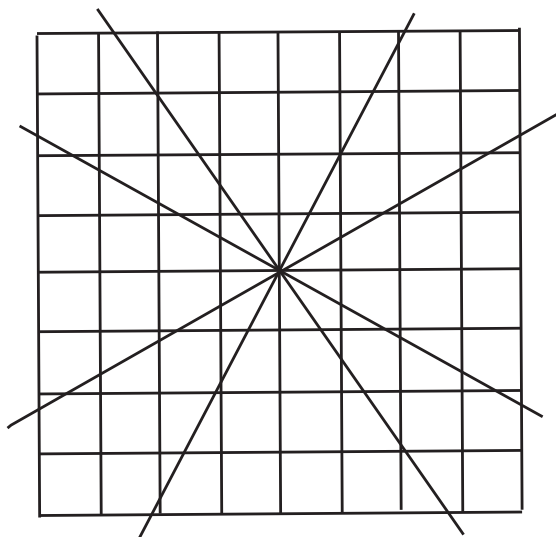


Figure 7: *2D representation of the 3D gridding process. Data from regular grids on randomly oriented central sections are interpolated onto a regular rectilinear 3D grid convenient for a fast Fourier transform routine.*

### 3 Forming a regular 3D diffracted intensity grid from randomly inclined central sections

We perform this 3D gridding operation by means of the MATLAB routine, *grid-data3*. This routine fits a hypersurface of the form  $w = f(x, y, z)$  to the irregularly spaced data from the randomly inclined central sections in reciprocal space, using a tessellation-based linear interpolation, which incorporates the method of Delaunay triangulation (Delaunay, 1934). The density of the uniform 3D grid points was chosen to ensure *oversampling* with respect to the Nyquist criterion for an object of the size of our test molecule. For the purposes of our present simulation, where the small test protein Chignolin is known to be smaller than a cube of linear dimension 16 Å, we take a reciprocal space sampling corresponding to the Nyquist frequency of a cube of double this linear dimension, namely 32 Å. That is, sampling frequency of the uniform rectilinear 3D reciprocal space grid is twice the Nyquist frequency corresponding to the diameter of the object in each of the three linear dimensions.

As the test was performed on simulated data, the efficiency of the determination of the relative orientations of the simulated diffraction patterns and of the gridding algorithm could be evaluated by comparing the diffraction data on the final uniform 3D Cartesian grid with diffraction intensities calculated directly on the same grid from the PDB atomic data. The usual X-ray R-factor was used to compare the two datasets. For our simulation of 630 diffraction patterns from the protein Chignolin, we obtained an R-factor value of 0.04, indicating a high fidelity for the the

orientation and gridding process.

## 4 Phasing of the diffraction data and the recovery of the 3D molecular electron density

The determination of the phases associated with the gridded diffraction data, and hence the 3D molecular electron density was performed by a combination of an iterative *oversampling* algorithm (Miao *et al.*, 2001), which successively imposes constraints/modifications of the electron density in real space through *object domain operations* (ODO) (Fienup, 1978; Oszlányi and Sütö, 2003) and in reciprocal space (Oszlányi and Sütö, 2004).

The 3D Fourier transform of the gridded diffraction *intensities* yields the 3D autocorrelation function of the molecular electron density. Since the extent of the autocorrelation map is twice that of the electron density map, the approximate spatial extent of the molecular electron density can be found directly from the diffraction intensities (Marchesini *et al.*, 2003).

A flow chart and pseudo code of our iterative phasing algorithm is shown in Fig. 8. The square roots of the gridded diffraction intensities are assumed proportional to the protein structure factors  $F_{\mathbf{q}}$ , say, where a reciprocal-space vector  $\mathbf{q}$  is defined by

$$\mathbf{q} = h\mathbf{b}_1 + k\mathbf{b}_2 + l\mathbf{b}_3 \tag{15}$$

where the unit vectors  $\mathbf{b}_i$  ( $i = 1, 2, 3$ ) of the reciprocal space are defined by the usual relationships

$$\mathbf{b}_i \cdot \mathbf{a}_j = \delta_{ij} \tag{16}$$

with respect to real-space unit vectors  $\mathbf{a}_j$  so chosen as to define a 3D volume expected to contain the molecule. Since the phases associated with these structure factors are initially unknown, we begin by assigning random phases to those structure factors  $F_{\mathbf{q}}$  corresponding to values of the Laue index  $l \geq 0$ . Assumption of Friedel's Law,

$$F_{-\mathbf{q}} = F_{\mathbf{q}}^* \tag{17}$$

then allows the assignment of complex structure factors for  $l < 0$ . An (inverse) FFT algorithm calculates an initial 3D electron density distribution, whose reality (in the mathematical sense) is assured by the above Friedel relationship amongst the structure factors. In general, the computed electron density is spread over a real-space volume larger than that of the molecule.

A support constraint is now applied in real space by setting to zero the electron density outside the volume expected to be occupied by the protein (Fienup, 1978). In

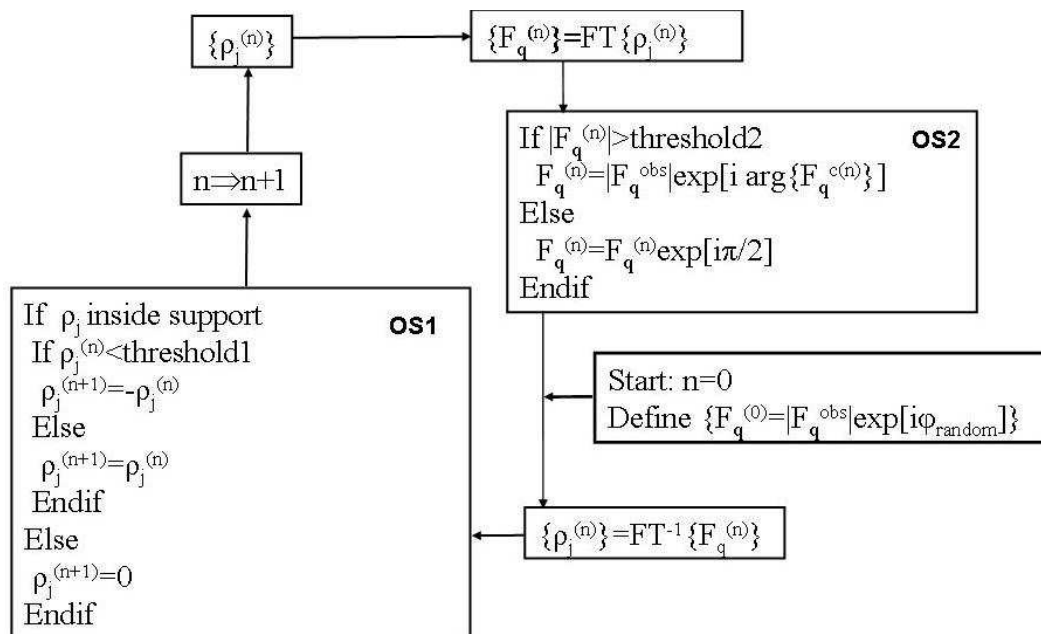


Figure 8: Flow chart and pseudo code of the iterative phasing algorithm

addition, the electron density within the expected volume of the protein is modified according to the *charge flipping* prescription of Oszlányi and Sütö (2003) (which was shown by Wu *et al.* (2004b) to be a special case of Fienup’s (1982) output-output algorithm with feedback parameter  $\beta = 2$ ). According to the charge flipping prescription, electron density values that exceed a certain threshold  $\delta$  are unmodified, while the signs of those below this threshold are reversed. The value of this threshold is chosen to optimize the progress of the algorithm, as monitored by an R-factor between the gridded “experimental” structure factors and those calculated from a Fourier transform of the electron density recovered by the algorithm. (The value for  $\delta$  taken in practice was typically around 10% of the maximum electron density.) A Fourier transform of the modified electron density specifies the same distribution in reciprocal space. The continued reality of this modified electron density ensures the resulting calculated structure factors have phases satisfying Friedel’s Law.

A different threshold is employed to divide the reciprocal-space amplitudes into *strong* and *weak* reflections. The magnitude of the threshold amplitude was again monitored by the same R-factor as for the real-space threshold above. The optimum division was found when 55% of the weakest reflections were classified as weak. A reciprocal-space constraint is applied to the strong reflections: their amplitudes (or moduli) are replaced by the square roots of the corresponding *measured* intensities, while retaining the phases from the Fourier transform operation. As for the weak reflections, their moduli are left unchanged, but their phases are shifted by  $\pi/2$ . The resulting set of complex structure factors is then subject to an inverse Fourier



Pair of Planes	Recovered/Actual $\Phi$	Recovered/Actual $\Theta$	Recovered/Actual $\Psi$
(0,1)	64.0/64.3	148.2/144.6	48.0/48.3
(0,2)	16.0/20.8	18.7/20.6	2.0/177.6
(0,3)	48.0/48.7	79.3/81.8	90.0/90.4
(0,4)	144.0/140.5	40.8/43.5	118.0/122.4
(0,5)	16.0/13.9	14.2/16.0	108.0/110.3
(0,6)		Not found	
(0,7)	174.0/174.2	138.9/138.2	100.0/99.6
(0,8)	90.0/90.0	92.3/87.9	168.0/169.7
(0,9)		Not found	
(0,10)		Not found	
Mean error	1.7	2.5	2.0

Table 4: Relative orientations of copies of a single molecule, as specified by a set of Euler angles  $\Phi$ ,  $\Theta$ , and  $\Psi$ , and the same angles recovered by the identified common lines between pairs of the diffraction patterns (reciprocal space planes) labeled 0 to 10, and analytical formulae described in the text. Also shown are the mean absolute errors in the determinations of these angles (all angles specified in degrees).

transformation, which yields another real-space electron distribution. This is modified in the same way as before, and the whole process repeated for several iterations.

This algorithm constrains the solution to be consistent with the measured intensities of the strong reflections in reciprocal space, and to the expected size of the object in real space. Subject to these constraints, it allows a thorough exploration of configuration space by iteratively modifying the phases of the weak reflections in reciprocal space and the signs of the small electron densities in real space.

## 5 Results for Noise-Free Simulations

We have tested the effectiveness of this algorithm on a set of 630 simulated diffraction patterns computed out to about 1 Å resolution from random orientations of the small synthetic protein Chignolin, simulated from the atomic elements and coordinate data taken from the Protein Data Bank, and atomic scattering factors calculated from the relevant Cromer-Mann coefficients (Cromer and Mann, 1968).

We then employed our common-line method to determine the Euler angles specifying the relative orientations of each of the simulated diffraction patterns. A typical comparison of the recovered angles with the known angles from the simulations is shown in Table 4.

Occasionally the common-line search (section 2) does not succeed in accurately finding the Euler angles  $\Phi$  and  $\Psi$  relating a pair of diffraction patterns. If an angle  $\Theta$

is calculated from such inexact values, the calculated argument of the arccosine in (8) may not lie in the range  $+1$  to  $-1$ , and thus may not yield a value for the Euler angle  $\Theta$ . As shown by Table 4, this is the case for the  $\Theta$  angle relating diffraction patterns (0,9) and (0,10). In such cases, we simply ignore the data in diffraction patterns 9 and 10. Proceeding this way, we were able to determine self-consistent solutions for the orientations of 401 out of the 630 diffraction patterns simulated. For our sample of 11 diffraction patterns, the mean accuracy of the Euler angle determination is about  $2^\circ$ . We used the data of the 401 correctly oriented diffraction patterns to assign intensities to an irregularly-spaced set of points in reciprocal space.

Is this sufficiently accurate? In order to answer this question one has to ask how accurately one needs to determine these angles to correctly assign intensities in each of the points of an oversampled 3D reciprocal-space grid. The required angular accuracy is thus determined by the angular extent of a reciprocal-space voxel of the highest resolution subtended at the origin of reciprocal space. Since the width of a reciprocal-space voxel is  $1/(2L)$  (Huldt, *et al.*, 2003), where  $L$  is a linear dimension of the molecule investigated, the angular resolution required is  $1/(2L)/(1/R) = R/(2L)$  radians, where  $R$  is the required resolution. For the example of the small protein modeled here, taking  $L=15 \text{ \AA}$  and  $R=1 \text{ \AA}$ , we may deduce that the required angular resolution is about  $1/30^{th}$  of a radian, or about  $2^\circ$ . Table 4 shows that this is achieved.

Application of the gridding algorithm of section 3 produced a set of diffraction intensities on such a uniform grid of points in 3D reciprocal space. Subsequent application of the iterative phasing algorithm of section 4 recovered the electron density distribution in the lower panel of Fig. 9 in about 65 iterations of the phasing algorithm.

For purposes of comparison, we also simulated the complex structure factors (amplitude and phase) on the same oversampled 3D grid of reciprocal-space points as used in the iterative phasing algorithm. An inverse Fourier transform of these (correct) complex structure factors recovered the protein electron density distribution in the upper panel of Fig. 9 at a resolution consistent with the extent of the diffraction data.

The recovered electron density is in reasonable agreement with that of the starting model, with a correlation coefficient of 0.7 between the two electron density distributions.

## 6 Effect of Shot Noise in Measured Diffraction Patterns

Even with radiation from an ultra-bright source such as an XFEL, the expected number of detected photons per pixel of a diffraction pattern from a single biomolecule is expected to be very small. Therefore, it is important to investigate the robustness of any algorithm to shot noise. We do this by assuming different mean photon counts

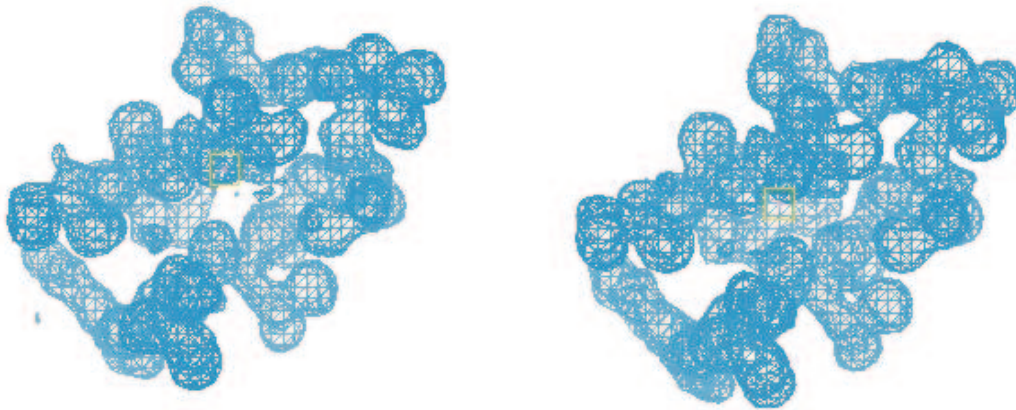


Figure 9: *Electron density of protein Chignolin (PDB Entry: 1UAO) to about 1 Å resolution. Upper panel from PDB model. Lower panel from multiple diffraction patterns of molecule in random orientations. The secondary structure is clearly visible.*

per pixel  $\bar{I}_0$  in the high resolution (or high-q) part of the diffraction pattern. If  $I_0$  is the expectation value of the photon count at any particular pixel, the actual number  $I$  of detected photons is determined by the Poisson distribution

$$p(I/I_0) = \frac{I_0^I}{I!} e^{-I_0} \quad (18)$$

where  $p(I/I_0)$  is the probability of measuring  $I$  photons. By comparing with the noise-free simulations, we investigated the effectiveness of the common-line algorithm in determining the relative Euler angles of the same diffraction patterns 0-10 of Table 4 for mean photon counts per pixel  $\bar{I}_0 = 100$  and  $\bar{I}_0 = 10$ .

The results of Table 4 were almost perfectly reproduced for  $\bar{I}_0 = 100$ , but there was substantial deterioration of the fidelity of the determined Euler angles for a mean photon count of  $\bar{I}_0 = 10$ , (Table 5).

In the same subset of 10 diffraction patterns, the algorithm was able to determine just 4 sets of relative Euler angles out of 10, with a mean angular accuracy of about  $3.5^\circ$ . We stated earlier that the required angular resolution is  $R/(2L) = 2^\circ$ , for 1 Å resolution. This may be relaxed to about  $4^\circ$ , if 2 Å resolution is accepted. However, the fact that the orientations of less than half the diffraction patterns could be determined suggests that a mean detected photon count/pulse/pixel of 10 is close to the practical lower limit for the direct use of a common-line approach. Of course, our current simulations were performed for a small protein, and we have not explicitly tested the dependence of this limit on protein size. However, it is of interest to note that a similar limit of counts per pixel is typical for cryo-electron microscopy of biological entities.

Pair of Planes	Recovered/Actual $\Phi$	Recovered/Actual $\Theta$	Recovered/Actual $\Psi$
(0,1)	68.0/64.3	150.6/144.6	52.0/48.3
(0,2)	14.0/20.8	18.1/20.6	4.0/177.6
(0,3)	48.0/48.7	85.6/81.8	92.0/90.4
(0,4)		Not found	
(0,5)		Not found	
(0,6)		Not found	
(0,7)	174.0/174.2	144.3/138.2	100.0/99.6
(0,8)		Not found	
(0,9)		Not found	
(0,10)		Not found	
Mean error	2.8	4.6	3.0

Table 5: Comparison of the determination of the relative Euler angles of the same 11 diffraction patterns as for the noise-free case of Table 4 for noisy diffraction patterns with mean photon count of 10 photons/pixel, with the (shot) noise modeled by a Poisson distribution

The significance of these results becomes apparent on comparing these values of  $\bar{I}_0$  with the estimated values of the same quantity under the usual assumptions of the incident beam flux from an XFEL for two different values of the focussed beam diameter  $D$ , as shown in Table 6.

In compiling this Table, we assumed that the molecule consists of  $N_{atom}$  non-H atoms (for the present purpose modeled as C atoms). We also distinguished between small-q and large-q scattering (where q is the scattering-induced momentum change of an incident photon) for the following reason. There is a large difference between the expected photon count for small-q and for high-q scattering. Put simply, all electrons in the sample scatter more or less *in phase* in the low-q regime, thereby giving rise to a scattered intensity proportional to  $N^2$ , where  $N$  is the number of electrons in

E(keV)	$\lambda$ (nm)	$\sigma_C$ (mm <sup>2</sup> /str. $\times 10^{-22}$ )		D ( $\mu$ m)	W (photons /mm <sup>2</sup> /pulse)	n (ph/pulse/pixel)	
		Small q	Large q			Small q	Large q
12.4	0.1	2.87	0.26	1	$2.6 \times 10^{18}$	50	$1.4 \times 10^{-4}$
				0.1	$2.6 \times 10^{20}$	5000	$1.4 \times 10^{-2}$

Table 6: Expected counts of detected photons/pulse/pixel for both small-q and large-q scattering by a 500 kDa protein with an XFEL source. E represents the photon energy,  $\lambda$  its wavelength,  $\sigma_C$  the typical differential scattering cross-sections for a C atom for small/large q, D the assumed diameter of a focussed beam incident on the sample, W the photon fluence, and n the estimated scattered photon count per pulse per detector pixel.

the sample ( $\simeq ZN_{atom}$ , with  $Z$  the average atomic number, and  $N_{atom}$  the number of atoms), while in the high-q regime, the scattered intensity is proportional to  $N$ .

Values for the differential scattering cross section of 12.4 keV X-rays by a C atom for small q and large q scattering were taken from the tables on elastic photon-atom scattering posted at the web site of the Lawrence Livermore National Laboratory (<http://www-phys.llnl.gov/Research/scattering>). Taking the effective width of a pixel as  $\Delta k = 2\pi/(2L)$  (Huldt *et al.*, 2003), where  $L$  is a linear dimension of the molecule, implies a reciprocal space pixel area of  $(\Delta k)^2 = 4\pi^2/(4L^2)$ . The solid angle subtended at the sample by each pixel is then

$$\Omega = (4\pi^2/4L^2)/k^2 = \lambda^2/4L^2 \text{ str.} \quad (19)$$

where  $k$  is the wavenumber of the radiation, and  $\lambda$  the wavelength. If  $a$  is the average spacing of non-H atoms, we may take  $(L/a)^3 \sim N_{atom}$ , or  $L \sim aN_{atom}^{1/3}$ . Substituting this value for  $L$  in (19), we deduce

$$\Omega \sim \frac{\lambda^2}{4a^2} N_{atom}^{-2/3} \text{ str.} \quad (20)$$

For high q, the measured photon count per pulse per pixel ( $n$ ) is estimated as

$$n \sim \Omega N_{atom} W \sigma_C = \frac{\lambda^2}{4a^2} N_{atom}^{1/3} W \sigma_C, \quad (21)$$

with a similar expression for low q, but with a  $N_{atom}^{4/3}$  dependence. Taking  $N_{atom} = 35,000$  (corresponding to a protein of approximately 500 kDa molecular weight), values for  $\lambda$ ,  $\sigma_C$ ,  $D$ , and  $W$  given in Table 6, and  $a$  taken as  $2 \text{ \AA}$ , we deduce the values for  $n$  for small/large momentum transfer q shown in the right-hand columns of Table 6.

It is important to note that, even for a focussed beam diameter of  $0.1 \mu\text{m}$ , the expected photon count per pixel for large-q data (needed for high-resolution structure determination) is approximately 3 orders of lower than the level at which the common-line method is able to reliably find the relative orientations of the diffraction patterns.

The estimates of Table 6 suggest that the photon counts in the low-q region of a single diffraction pattern of a large protein may be high enough to render the effects of shot noise negligible. However, it is unlikely that structural information directly available from low-q data will yield anything more than the overall shape of the scattering object, as in the technique of small angle X-ray scattering (SAXS). It is an open question whether a coarse orientating of patterns, which may be performed with the low-q data, will help to orientate entire diffraction patterns sufficiently accurately to exploit the high-q data for high-resolution structure determination.

## 7 Discussion

The ability to record and sort 2D diffraction patterns from individual molecules is important for a number of reasons. First and most obvious is the elimination of the need for crystals. Second, and in our view equally important, is the potential to sort and separate diffraction patterns from different molecules or different molecular conformations in the beam prior to structure recovery. The fact, for example, that 2D diffraction patterns from different molecules do not have common lines might allow the diffraction patterns to be separated into sets before further analysis, with each set designating a different type of molecule or molecular conformation.

This paper has been concerned with developing an algorithm to determine the structure of a single scattering entity (such as a protein, or nanoparticle) from multiple diffraction patterns due to scattering from unknown random orientations of identical copies of the object. We have shown that an adaptation of a “common-line” algorithm from 3D electron microscopy/tomography is able to accomplish this task for noise-free diffraction patterns in the flat Ewald sphere limit. There is little doubt that an extension of such a method to curved common-lines will similarly enable structure determination from low-noise diffraction patterns at  $\sim 1 \text{ \AA}$  wavelengths characteristic of currently planned XFELs (Hajdu *et al.*, 2000; Abela *et al.*, 2007).

Of much greater concern is that fact that, even with the most powerful XFELs currently envisaged, the expected number of scattered photons per high-q pixel of a molecular diffraction pattern from a single radiation pulse is far too low for the alignment approaches proposed so far. The common-line method relies on identifying similar intensity distributions along *single lines* in two low-intensity (and thus high-noise) diffraction patterns. As such, it is hardly surprising that it is very sensitive to noise. Our conclusion is that such a method requires a mean photon count of at least 10 per pixel in the high-q region of a diffraction pattern, about 3 orders of magnitude greater than expected from a proposed experiment with an XFEL (Table 6).

We note that in the proposed experiments, the minimum photon count per diffraction pattern orientation is not determined by the minimum required to reconstruct a satisfactory 3D image of the object from projections of known orientations, as in conventional tomography, but rather by the need for correct classification and assembly of a 3D diffraction volume from data in diffraction patterns alone. The minimum photon count in the former case may be quite low, since the dose fractionation theorem for 3D electron microscopy/tomography (Hegerl & Hoppe, 1976; McEwen, Downing, & Glaeser, 1985) states that “A three-dimensional reconstruction requires the same integral dose as a conventional two-dimensional micrograph provided that the level of significance and resolution are identical”. This suggests that if there are  $M$  projections (or in our case, diffraction patterns) the photon count per pixel required for an equally successful 3D reconstruction will be just  $1/M$  of that for a single projected image (in our case a single diffraction pattern). In the absence of orientational information, this theorem does not help, because a much higher photon count (about 10 photons/pixel per orientational class) is needed for the successful assembly of a

3D diffraction volume suitable for structure solution. In short, the minimum photon count for correct classification and orientation is much higher than that needed for structure recovery of a single biomolecule.

We now consider the possibility of classifying measured diffraction patterns into sets of similar orientations, and averaging their intensities to improve their signal-to-noise ratios. Bortel and Faigel (2007) find that successful classification of measured diffraction patterns of a protein modeled by 35,000 C atoms requires an incident photon fluence of  $10^{28} \text{ m}^{-2}/\text{pulse} = 10^{22} \text{ mm}^{-2}/\text{pulse}$ . Comparison with our Table 6 shows that this is  $100\times$  the fluence expected from an XFEL beam focused down to a  $0.1 \mu\text{m}$  diameter spot. Even if a more efficient method of classification were found, Table 6 indicates that the number of photons expected per high-resolution pixel of the diffraction pattern is  $\sim 10^{-2}$ , approximately 3 orders of magnitude smaller than that needed for the common-line method. This suggests the need for the summation of the data from about 1000 diffraction patterns per orientational class. Since Bortel and Faigel also find that at about  $10^6$  classes are required for faithful recovery of the structure of such a molecule (assumed to be  $100 \text{ \AA}$  in diameter) to  $3 \text{ \AA}$  resolution, it will be necessary to measure  $\sim 10^9$  diffraction patterns. Assuming photon pulse and read-out rates of 100 Hz, this would require  $\sim 10^7$  seconds, or several months of continuous beam time for a single experiment.

We note that the classification problem is not eased for an even larger scattering object, such as a virus or nanoparticle. Eq. (21) suggests that the number of photons per detector pixel varies as  $N_{atom}^{1/3}$ . Thus, a scattering entity modeled by  $N_{atom}=10^6$  C atoms, would scatter 3 times as many photons into each pixel. However, Bortel and Faigel (2007) estimate the number of required orientational classes for the structure solution of such an entity (assumed to be of  $300 \text{ \AA}$  diameter) to  $3 \text{ \AA}$  resolution is  $2\times 10^7$ , an extra factor of about 30 or so over the 500 kDa protein. Thus the total number of diffraction patterns required, and hence time for data collection, would be expected to increase to  $10^8$  seconds, i.e. several years for a single experiment.

Assembling a 3D intensity distribution from the low-intensity diffraction patterns from single molecules obtainable from single pulses of an XFEL may not be practical with the common-line method, the only approach mentioned in the literature so far (see e.g. the Technical Design Report of the European XFEL, Abela *et al.*, 2007). This calls for the development of entirely new algorithms that perform structure solution by simultaneously acting on all the data of all measured diffraction patterns. Two such approaches have been suggested by the present authors (Ourmazd *et al.*, 2007; Saldin *et al.*, 2007) and will be the subject of forthcoming publications <sup>1</sup>.

---

<sup>1</sup>An alternative approach has been proposed by Spence *et al.* (2005) for improving the signal-to-noise ratio, in which the orientational alignment of the molecules is controlled by means of crossed laser beams.

## 8 Conclusions

We have presented the first demonstration of an integrated algorithm to determine the electron density of a particle or large biomolecule, such as a protein, from a collection of 2D diffraction patterns, each from a molecule in an unknown random orientation, as expected from the proposed X-ray scattering experiments with XFEL sources. The method involves first determining the relative orientations of the different 2D diffraction patterns, interpolating the data onto a regular 3D Cartesian grid in reciprocal space at a sampling rate higher than the Nyquist frequency for the size of the molecule, determining the phases associated with the measured amplitudes, and hence deducing the 3D electron density of the molecule or nanoparticle. There are significant differences with similar algorithms developed previously for 3D electron microscopy, due to the absence of direct phase information, and the ambiguities due to Friedel’s Law. We have shown how these difficulties may be overcome, even in the limit of a flat Ewald sphere, by the imposition of appropriate consistency conditions. These enable the determination of the relative orientations of the diffraction patterns, and hence the molecular structure, to within the usual enantiomeric uncertainty.

We have tested the algorithm with a computer simulation for a model protein, at an X-ray wavelength short enough to justify the flat Ewald sphere approximation, with and without Poisson noise for the detected photons. Adaptation of this algorithm to take account of curved common lines can readily extend the applicability of this approach to longer X-ray wavelengths.

Our simulations have highlighted an important limitation of a common-line method for finding the relative orientations of diffraction patterns from random orientations of a sample. Such methods depend on comparing the intensity distributions along particular lines in two diffraction patterns, thus using only a very small fraction of the available data for each orientation determination. They are consequently very sensitive to noise.

We find that the common-line method ceases to work reliably for mean photon counts per pixel below about 10 in the high- $q$  part of a diffraction pattern. These regions contain the high-resolution information needed to resolve the secondary structure of a protein. Since the scattering by a typical (500 kDa) protein of a pulse from a planned XFEL beam focused to a spot of  $0.1\ \mu\text{m}$  diameter is expected to produce some  $1000\times$  fewer photons per detector pixel, the use of a common-line method would seem to necessitate the classification and averaging of at least 1000 low-intensity diffraction patterns per orientational class to correctly assemble the scattered intensity distribution in 3D reciprocal space.

The method of classifying diffraction patterns into orientational classes examined by Bortel and Faigel (2007) requires at least  $100\times$  the anticipated XFEL fluence. Even if superior classification methods were devised, the determination of the structure of a  $100\ \text{\AA}$ -wide molecule to  $3\ \text{\AA}$  resolution would require about  $10^6$  orientational classes (Bortel and Faigel, 2007). Assuming pulse and read-out rates of 100Hz, data



collection for a 500 kDa protein would require several months of continuous beam time.

We thank Veit Elser, Leonard Feldman, Paul Fuoss, John Spence, and Brian Stephenson for helpful discussions.

## References

- Abela, R. *et al.* (2007). *The European X-Ray Free-Electron Laser: Technical Design Report*, [http://xfel.desy.de/tdr/index\\_eng.html](http://xfel.desy.de/tdr/index_eng.html), edited by Altarelli, M. *et al.*, 401-420.
- Bortel, G. & Faigel, G. (2007). *J. Struct. Biol.* **158**, 10-18.
- Chapman, H. N., Barty, A., Marchesini, S., Noy, A., Hau-Riege, S. P., Cui, C., Howells, M. R., Rosen, R., He, H., Spence, J. C. H., Weierstall, U., Beetz, T., Jacobsen, C., & Shapiro, D. (2006). *J. Opt. Soc. Am.* **23**, 1179-1200.
- Chapman, H. N. (2007), private communication.
- Cooley, J. W. & Tukey, J. W. (1965). *Math. of Comp.* **19**, 297-301.
- Cramer, P., Bushnell, D. A., & Kornberg, R. D. (2001). *Science* **292**, 1863-1876.
- Cromer, D. T. & Mann, J. B. (1968). *Acta Cryst.* **A24**, 321-324.
- Delaunay, B. (1934). *Isvetia Akademii Nauk SSSR, Otdelenie Matematicheskikh Estestvennykh i Nauk* **7**, 793-800.
- Elser, V. (2003). *J. Opt. Soc. Am. A* **20**, 40-55.
- Gnatt, A. L., Cramer, P., Fu, J., Bushnell, D. A., & Kornberg, R. D. (2001). *Science* **292**, 1876-1882.
- Farrow, N. A. & Ottensmeyer, F. P. (1992). *J. Opt. Soc. Am. A* **9**, 1749-1760.
- Fenn, J. B. (2002). *J. Biomolecular Techniques* **13**, 101-118.
- Fienup, J. R. (1978), *Opt. Lett.* **3**, 27-29.
- Fienup, J. R. (1982), *Appl. Opt.* **21**, 2758-2769.
- Frank, J. (2006). *Three-Dimensional Electron Microscopy of Macromolecular Assemblies*. Oxford University Press.

- Fung, R., Shneerson, V. L., Lyman, P. F., Parihar, S. S., Johnson-Steigelman, H. T., & Saldin, D. K. (2007). *Acta Cryst.* **A63**, 239-250.
- Goncharov, A. B., Vainshtein, B. K., Ryskin, A. I., & Vagin, A. A. (1987). *Sov. Phys. Crystallogr.* **32**, 504-509.
- Hajdu, J., Hodgson, K., Miao, J., van der Spoel, D., Neutze, R., Robinson, C. V., Faigel, G., Jacobsen, C., Kirz, J., Sayre, D., Weckert, E., Materlik, G., & Szöke, A. (2000). *Structural Studies of Single Particles and Biomolecules, in LCLS: The First Experiments*, [http://www-ssrl.slac.stanford.edu/lcls/papers/lcls\\_experiments\\_2.pdf](http://www-ssrl.slac.stanford.edu/lcls/papers/lcls_experiments_2.pdf), 35-62.
- Hegerl, R. & Hoppe, W. (1976). *Z. Naturforschung* **31a**, 1717-1721.
- Huldt, G., Szöke, A., & Hajdu, J. (2003). *J. Struct. Biol.* **144**, 218-227.
- Jurek, Z., Faigel, G. & Tegze, M. (2004). *Eur. Phys. J.* **29**, 217-229.
- Kumpf, C., Marks, L. D., Ellis, D., Smilgies, D., Landemark, E., Nielsen, M., Feidenhans'l, R., Zegenhagen, J., Bunk, O., Zeysing, J. H., Su, Y. & Johnson, R. L. (2001). *Phys. Rev. Lett.* **86**, 3586-3589.
- Marchesini, S., He, H., Chapman, H. N., Hau-Riege, S. P., Noy, A., Howells, M. R., Weierstall, U. & Spence, J. C. H. (2003). *Phys. Rev. B* **68**, 140101(R).
- McEwen, B. F., Downing, K. H., & Glaeser, R. M. (1995). *Ultramicroscopy* **60**, 357-373.
- Miao, J., Hodgson, K., & Sayre D. (2001). *Proc. Nat. Acad. Sci. U.S.A.* **98**, 6641-6645.
- Millane, R. P. (2003). *Proc. Oceans 2003, CD ROM, IEEE* 2714-2719.
- Neutze, R., Wouts, R., van der Spoel, D., Weckert, E., & Hajdu, J. (2000). *Nature* **406**, 752-757.
- Normille, D. (2006). *Science* **314**. 751-752.
- Oszlányi, G. & Süto, A. (2003). *Acta Cryst.* **A60**, 134-141.
- Oszlányi, G. & Süto, A. (2004). *Acta Cryst.* **A61**, 147-152.
- Ourmazd, A., Fung, R., Shneerson, V. L., and Saldin, D. K. (2007). *Coherence 2007*, International Workshop on Phase Retrieval and Coherent Scattering, Asilomar, California.

Saldin, D. K., Shneerson, V. L., Fung, R., Ourmazd, A. (2007). *Coherence 2007*, International Workshop on Phase Retrieval and Coherent Scattering, Asilomar, California.

Shapiro, D., Thibault, P., Beetz, T., Elser, V., Howells, M., Jacobsen, C., Kirz, J., Lima, E., Miao, H., Nieman, A. M., & Sayre, D. (2005). *Proc. Nat. Acad. Sci. U.S.A.* **102**, 15343-15346.

Solem, J. C. & Baldwin, G. C. (1982). *Science* **218**, 229-235.

Spence, J. C. H., Schmidt, K., Wu, J.S., Hembree, G., Weierstall, U., Doak, B., & Fromme, P. (2005). *Acta Cryst.* **A61**, 237-245.

Thibault, P., Elser, V., Jacobsen, C., Shapiro, D., & Sayre, D. (2006). *Acta Cryst.* **A62**, 248-261.

van Heel, M. (1987). *Ultramicroscopy* **21**, 111-124.

Williams, G. J., Pfeifer, M. A., Vartanyants, I. A., & Robinson, I. K. (2003). *Phys. Rev. Lett.* **90**, 175501.

Wu, J. S., Spence, J. C. H., O'Keeffe, M. A., & Groy, T. L. (2004a). *Acta Cryst.* **A60**, 326-330.

Wu, J. S., Weierstall, U., Spence, J. C. H., & Koch, C. T. (2004b). *Opt. Lett.* **29**, 2737-2739.

Wu, J., Weierstall, U., & Spence, J. C. H. (2005). *Nature Materials* **4**, 912-916.